Makara J. Technol. 18/1 (2014), 41-50
doi: 10.7454/mst.v18i1.2940

Performance Evaluation of an Optimized Floating Breakwater in Oblique Waves with a Higher-Order Boundary Element Method

Faisal Mahmuddin[1*] and Masashi Kashiwagi[2]

1. Department of Naval Architecture, Faculty of Engineering, Universitas Hasanuddin, Makassar 90245, Indonesia
2. Naval Architecture and Ocean Engineering Department, Osaka University, 2-1 Yamadaoka, Suita, Osaka 565-0871, Japan

**e-mail: f.mahmuddin@gmail.com*

Abstract

In the previous study, the optimal performance of a two-dimensional (2D) floating breakwater shape was obtained. The performance of this shape was also confirmed with a model experiment in a towing tank. Moreover, the shape's performance in three dimensions (3D) was investigated in a subsequent study. However, to predict the shape's performance in a real application more accurately, the shape's characteristics in oblique waves must also be evaluated. In this study, the performance and characteristics of the model (hydrodynamic forces, body motions, wave elevations, and drift forces) are computed using a higher-order boundary element method (HOBEM). The HOBEM, which is based on the potential flow theory and uses quadratic representation for quadrilateral panels and velocity potentials, can be used to obtain more accurate results with fewer panels compared to the conventional panel method (CPM). The computational accuracy is confirmed by using Haskind-Newman and energy conservation relations. In this study, 3D wave effects were verified, and the body motions were much smaller compared to the 2D case. In addition, although the performance in terms of wave elevations depends on the measurement positions, the optimal performance obtained in the 2D case can be realized for a longer body length.

Abstrak

Evaluasi Performa Sebuah Pemecah Gelombang Terapung yang Telah Dioptimasi pada Gelombang Datang Miring dengan Metode Elemen Batas Orde Tinggi (HOBEM). Pada penelitian sebelumnya, sebuah bentuk model pemecah gelombang terapung dalam kasus 2D yang mempunyai performa optimal telah didapatkan. Performa dari bentuk ini dikonfirmasi dengan melakukan sebuah eksperimen model pada kolam uji. Selain itu, performa model tersebut telah pula diinvestigasi untuk kasus 3D pada penelitian berikutnya. Namun demikian, untuk dapat memprediksi performa model tersebut secara lebih akurat saat penerapannya di dunia nyata, maka menjadi sangat penting untuk mengevaluasi karakteristik dan performa model tersebut pada kasus gelombang datang miring. Pada penelitian ini, performa dan karakteristik dari model yang dimaksud berupa gaya hidrodinamika, olah gerak, elevasi gelombang dan gaya *drift* ditentukan dengan menggunakan metode elemen batas orde tinggi atau HOBEM. HOBEM yang dikembangkan berdasarkan teori potensial aliran dan menggunakan representasi kuadratik untuk panel kuadrilateral dan potensial kecepatan, dapat digunakan untuk memperoleh hasil yang lebih akurat dengan menggunakan jumlah panel yang lebih sedikit dibandingkan dengan metode panel konvensional. Keakuratan perhitungan dapat dikonfirmasi dengan menggunakan relasi Haskind-Newman and hukum konservasi energi. Dari penelitian ini, efek gelombang 3D dapat diverifikasi lebih lanjut dan olah gerak model ditunjukkan menjadi jauh lebih kecil dibandingkan pada kasus 2D. Selain itu, dapat pula disimpulkan dari hasil perhitungan bahwa meskipun performa model berupa elevasi gelombang akan tergantung dari posisi pengukuran, akan tetapi performa optimal yang telah didapatkan sebelumnya pada kasus 2D dimensi dapat direalisasi kembali untuk model yang cukup panjang.

Keywords: 3D wave effects, floating breakwater, higher order boundary element method (HOBEM), oblique waves, performance evaluation

1. Introduction

High demand and the wide application of a floating type of breakwater has attracted the attention of many researchers. The main objectives of their research are increasing the performance of this type of breakwater, which is commonly measured by the number of incident waves transmitted by and reflected from the body.

Therefore, the performance of several model shapes have been evaluated and tested numerically and/or experimentally such as the Y-shaped model [1], pi-shaped model [2], diamond-shaped model [3], pontoon type model [4,5], cage-shaped model [6], and many other shapes.

Not only the shapes but also the evaluation methods used in the performance evaluation are diverse. For example, Kashiwagi et al. applied the boundary element method (BEM) [7], Rahman et al. implemented the volume of fluid method [8], Koshizuka et al. used the moving particle semi-implicit method [9], and Koo adopted a nonlinear numerical wave tank (NWT) technique [10]. Each method has advantages and disadvantages. The method implemented by Kashiwagi et al. is based only on linear theory but is practical to use with less computation time. The methods used by Rahman et al., Koshizuka et al., and Koo treated nonlinear phenomena but with higher computational costs.

In a study conducted by Mahmuddin and Kashiwagi, an optimization method called the genetic algorithm (GA) was adopted to obtain a two-dimensional (2D) model shape with optimal performance [11]. A real model was manufactured and tested in a towing tank at Osaka University, Japan, to verify the model's performance. Relatively good agreement can be obtained with some discrepancies in the natural frequencies of roll motion, especially when the body is free to respond to the incident wave. These discrepancies could be attributed to viscous damping, which is not considered in the potential flow theory framework.

In a subsequent study conducted by Kashiwagi and Mahmuddin, the performance of this model in the three-dimensional (3D) case was also evaluated using a higher-order boundary element method (HOBEM) [12]. The influence of 3D wave effects on the body motions was small, and the free surface elevation was spatially three dimensional even near the middle of a longer body.

In those previous studies [11,12], the incident wave direction was defined to be perpendicular to the body. However, since in the ocean waves come from all directions, the characteristics and performance in oblique waves must be evaluated so that the performance in real applications can be predicted more comprehensively.

The performance of a floating breakwater model in oblique waves has also been investigated by several researchers. For example, Dalrymple et al. evaluated the performance of a floating breakwater for porous structures [13], Cho et al. evaluated the performance of the flexible-membrane wave barrier [14], while Wu et al. and Zheng et al. examined floating rectangular structures [15,16].

In the present study, HOBEM will be used again to compute the characteristics and performance of the model for two incident wave angles. In the HOBEM, the body surface below the free surface is divided into many quadrilateral panels. Each panel on the body surface and the unknown velocity potentials on that panel are represented by 9-node quadratic Lagrangian elements.

Consequently, greater accuracy can be obtained using fewer panels compared to the conventional constant panel method (CPM). Using fewer panels in the computation shortens the computation time. Another advantage of the HOBEM is that the solid angle is computed numerically while it is assumed to be constant in the CPM.

However, in the HOBEM, dividing the body into panels is more difficult compared to the CPM. This is because in the HOBEM, two types of nodes must be used, local nodes and global nodes, while only global nodes are used in the CPM. In both methods, numerical accuracy can be confirmed with Haskind-Newman and energy conservation relations.

In this study, 3D wave effects are confirmed and understood by observing wave field plots. Moreover, small body motions compared to the corresponding 2D shape are also observed. Although the performance in terms of wave elevation especially wave transmission depends on the measurement positions, the optimal performance obtained in the 2D case can be realized for a longer body length.

2. Methods

Mathematical formulation. The present study is actually concerned with developing floating breakwaters that have arbitrary shapes and high performance in wave reflection. However, considering the current problem where the body shape is obtained by extruding a 2D model shape, the body shapes can be assumed to be symmetric in terms of the *y*-*z* plane but asymmetric in terms of the *x*-*z* plane. As a result, the coordinate system shown in Fig.1 is adopted.

The origin of the coordinate system is placed at the center of the body and on the undisturbed free surface, and the *z*-axis is taken positive vertically downward. The water depth is assumed to be infinite. The regular wave is considered to be incoming with incident angle β regarding the negative x-axis as shown in Fig. 1. Thus β = -90 degrees means the beam wave incoming from the positive y-axis.

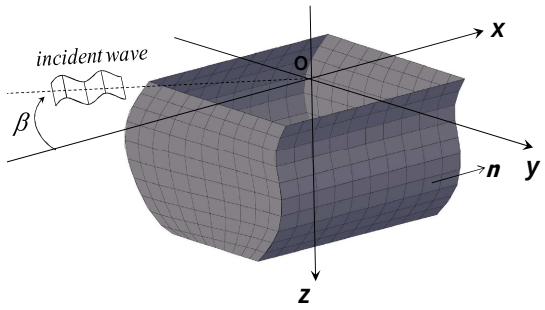

Figure 1. Coordinate System in the 3D Analysis

Under the assumption of incompressible and inviscid flow with irrotational motion, the velocity potential can be introduced, satisfying Laplace's equation as the governing equation. The boundary conditions are linearized, and all oscillatory quantities are assumed to be time-harmonic with circular frequency ω. Applying the superposition principle, the velocity potential can be expressed as a summation of the incident-wave potential ϕ_0 and the disturbance potential ϕ as follows:

$$\Phi(x,y,z,t) = \mathrm{Re}\left[\left\{\phi_0(x,y,z)+\phi(x,y,z)\right\}e^{i\omega t}\right] \tag{1}$$

where ϕ_0 can be given explicitly as

$$\phi_0(x,y,z) = \frac{g\zeta_a}{i\omega}e^{-Kz-iK(x\cos\beta+y\sin\beta)} \tag{2}$$

with g the acceleration of gravity, ζ_a the amplitude of incident wave, and K the wave number given by $K=\omega^2/g$. Furthermore, the disturbance potential ϕ can be decomposed in the following form:

$$\phi(x,y,z) = \frac{g\zeta_a}{i\omega}\left[\phi_7(x,y,z) - K\sum_{j=1}^{6}\frac{X_j}{\zeta_a}\phi_j(x,y,z)\right] \tag{3}$$

where ϕ_7 denotes the scattering potential in the diffraction problem, and ϕ_j is the radiation potential in the j-th mode of the body motion with complex amplitude X_j. The six modes of motion considered in the present study are surge ($j=1$), sway ($j=2$), heave ($j=3$), roll ($j=4$), pitch ($j=5$), and yaw ($j=6$). For the diffraction problem, the sum of $\phi_0+\phi_7$ is denoted as ϕ_D, which is referred to as the diffraction potential.

The governing equation and the boundary conditions to be satisfied can be summarized as follows:

$$[L] \quad \nabla^2\phi_j = 0 \qquad \text{for } z \ge 0 \tag{4}$$

$$[F] \quad \frac{\partial\phi_j}{\partial z} + K\phi_j = 0 \qquad \text{on } z=0 \tag{5}$$

$$[H] \quad \frac{\partial\phi_j}{\partial n} = \begin{cases} n_j & (j=1\sim 6) \\ 0 & (j=D) \end{cases} \quad \text{on } S_H \tag{6}$$

$$[B] \quad \frac{\partial\phi_j}{\partial z} = 0 \qquad \text{as } z\to\infty \tag{7}$$

and an appropriate radiation condition of outgoing waves must be satisfied for $j=1\sim 7$. Here, S_H denotes the body wetted surface and n_j the j-th component of the normal vector, defined as positive when directing out of the body and into the fluid.

By using Green's theorem, the governing differential equations of this problem are turned into integral equations on the boundary. That boundary surface can be only the body surface S_H by introducing the free-surface Green function, and the resulting integral equations can be written in the form

$$C(P)\phi_j(P) + \iint_{S_H}\phi_j(Q)\frac{\partial}{\partial n_Q}G(P;Q)\,dS(Q) = \begin{cases} \iint_{S_H} n_j(Q)G(P;Q)\,dS(Q) & j=1\sim 6 \\ \phi_0(P) & j=D \end{cases} \tag{8}$$

where $C(P)$ is the solid angle, $P=(x,y,z)$ is the field point, and $Q=(x',y',z')$ is the integration point on the body surface. $G(P;Q)$ is the free-surface Green function satisfying the linearized free-surface and radiation conditions, which can be expressed as

$$G(P;Q) = -\frac{1}{4\pi}\left(\frac{1}{r}+\frac{1}{r_1}\right) - \frac{K}{2\pi}G_W\left(R, z+z'\right) \tag{9}$$

where

$$\left.\begin{matrix} r \\ r_1 \end{matrix}\right\} = \sqrt{(x-x')^2+(y-y')^2+(z\mp z')^2} \equiv \sqrt{R^2+(z\mp z')^2} \tag{10}$$

$$G_W(R,z) = -\frac{2}{\pi}\int_0^\infty \frac{k\sin kz + K\cos kz}{k^2+K^2}K_0(kR)\,dk - i\pi e^{-Kz}H_0^{(2)}(KR) \tag{11}$$

Here, $K_0(kR)$ denotes the second type of modified Bessel function of the zero-th order and $H_0^{(2)}(KR)$ the second type of Hankel function of the zero-th order.

Higher-order boundary element method. For high accuracy, the integral equation shown above was numerically solved with HOBEM, described in Kashiwagi [17]. The body surface is discretized into many quadrilateral panels. According to the iso-

parametric representation, the body surface and the unknown velocity potential on each panel are represented with 9-point quadratic shape functions $N_k(\xi,\eta)$ $(k=1\sim 9)$ as follows:

$$\{x,y,z\}^T = \sum_{k=1}^{9} N_k(\xi,\eta)\{x_k,y_k,z_k\}^T \tag{12}$$

$$\phi(x,y,z) = \sum_{k=1}^{9} N_k(\xi,\eta)\phi_k \tag{13}$$

where (x_k,y_k,z_k) are local coordinates at 9-nodal points on a panel under consideration, and likewise, ϕ_k denotes the value of the velocity potential (which is to be determined) at the 9-nodal points of a panel.

The shape function in Eqs. (12) and (13) for a quadrilateral panel can be expressed in the following form

$$\left.\begin{aligned} N_k &= \frac{1}{4}\xi(\xi+\xi_k)\eta(\eta+\eta_k) \quad \text{for } k=1\sim 4 \\ N_5 &= \frac{1}{2}\eta(\eta-1)(1-\xi^2), \quad N_6 = \frac{1}{2}\xi(\xi+1)(1-\eta^2) \\ N_7 &= \frac{1}{2}\eta(\eta+1)(1-\xi^2), \quad N_8 = \frac{1}{2}\xi(\xi-1)(1-\eta^2) \\ N_9 &= (1-\xi^2)(1-\eta^2) \end{aligned}\right\} \tag{14}$$

where index k denotes the local node number $(k=1\sim 9)$, as shown in Figure 2.

The normal vector on the body surface (each panel) can be computed with differentiation of the shape function as follows:

$$\boldsymbol{n} = \frac{\boldsymbol{a}\times\boldsymbol{b}}{|\boldsymbol{a}\times\boldsymbol{b}|}, \quad \boldsymbol{a} = \left(\frac{\partial x}{\partial\xi},\frac{\partial y}{\partial\xi},\frac{\partial z}{\partial\xi}\right), \quad \boldsymbol{b} = \left(\frac{\partial x}{\partial\eta},\frac{\partial y}{\partial\eta},\frac{\partial z}{\partial\eta}\right) \tag{15}$$

Through a series of substitutions, the boundary integral equations can be recast in a series of algebraic equations for the velocity potentials at nodal points consisting of panels. The results can be expressed in the form

$$C_m\phi_m + \sum_{\ell=1}^{NT} D_{m\ell}\phi_\ell = \begin{cases} \sum_{n=1}^{N} S_{mn}^j & j=1\sim 6 \\ \phi_0(P_m) & m=1\sim NT \end{cases} \tag{16}$$

where

$$D_{m\ell} = \iint_{S_n} N_k(\xi,\eta)\frac{\partial G(P_m;Q)}{\partial n_Q}\left|J(\xi,\eta)\right| d\xi d\eta \tag{17}$$

$$S_{mn}^j = \iint_{S_n} n_j(Q)G(P_m;Q)\left|J(\xi,\eta)\right| d\xi d\eta \tag{18}$$

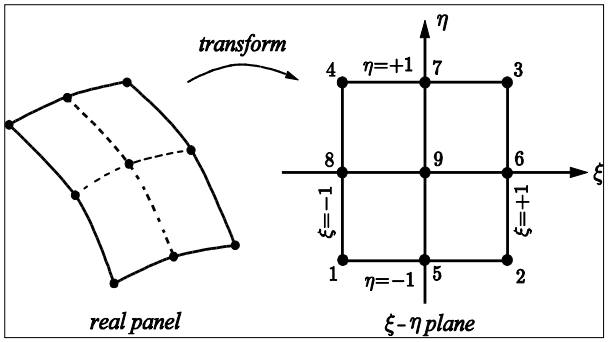

Figure 2. Quadrilateral 9-node Lagrangian Element

and index n denotes the serial n-th panel, index m the global serial number of nodal points, and $\ell=(n,k)$ is also the serial number of nodal points associated with (to be computed from) the k-th local node within the n-th panel. $|J(\xi,\eta)|$ in Eqs. (17) and (18) denotes the Jacobian in the variable transformation. NT denotes the total number of nodal points, and thus, Eq. (16) is a linear system of simultaneous equations with dimensions $NT\times NT$ for the unknown velocity potentials at the nodal points. The solid angle C_m in Eq. (16) is computed numerically by considering the equi-potential condition that a uniform potential applied over a closed domain produces no flux and, thus, zero normal velocities over the entire boundary.

The free-surface Green function, given by Eq. (11), can be computed efficiently by combining several expressions such as the power series, asymptotic expansions, and recursion formulae; the subroutine is available in Kashiwagi et al. [18].

In actual numerical computations, a few additional field points are considered on the interior free surface of a floating body to remove the irregular frequencies. At these field points, the value of solid angle C_m in Eq. (16) must be zero; this technique is adopted following the idea Haraguchi and Ohmatsu established for 2D problems [19]. The resultant over-constraint simultaneous equations are solved with the least-squares method.

Hydrodynamic forces. Once the velocity potentials on the body surface are determined, computing the hydrodynamic forces is straightforward. The results are written in the form

$$F_{ij} = -\rho\iint_{S_H}\phi_j\, n_i\, dS \equiv A_{ij} - \frac{i}{\omega}B_{ij} \tag{19}$$

$$E_j = \rho g\zeta_a\iint_{S_H}\phi_D\, n_j\, dS \tag{20}$$

where F_{ij} is the radiation force in the i-th direction due to the j-th mode of motion, and its real and imaginary

parts are the added mass A_{ij} and damping coefficient B_{ij} . E_j in Eq. (20) denotes the wave-exciting force. These quantities are expressed in terms of the origin of the coordinate system shown in Fig. 1, and can be combined to obtain corresponding quantities expressed regarding the center of gravity, which will be used in establishing the motion equations.

The body motion equations regarding the center of gravity can be established in a matrix form as follows:

$$\sum_{j=1}^{6} X_j^G \left\{ -K\left(M_{ij}\,\delta_{ij} + F_{ij}^G\right) + C_{ij}^G \right\} = E_i^G \quad \text{for } i = 1 \sim 6 \tag{21}$$

The superscript *G* represents the quantities linked to the center of gravity. M_{ij} denotes the generalized mass matrix, δ_{ij} is Kroenecker's delta, and C_{ij}^G is the restoring-force coefficients due to the static pressure. By solving these coupled motion equations, the complex motion amplitude X_j^G can be determined, and then the corresponding complex amplitude of the origin of the coordinate system X_j $(j = 1 \sim 6)$ can be obtained from

$$\left.\begin{aligned} X_j &= X_j^G + \varepsilon_{jkl}\,(x_G)_k\, X_{l+3}^G \\ X_{j+3} &= X_{j+3}^G \end{aligned}\right\} \quad (j = 1 \sim 3) \tag{22}$$

where ε_{jkl} denotes the alternating tensor for the outer product of the vectors and $(x_G)_k$ $(k = 1 \sim 3)$ the ordinates of the center of gravity.

The numerical accuracy can be confirmed by checking the Haskind-Newman relation for the wave-exciting force and the energy-conservation relation for the damping coefficient. These relations are expressed as

$$E_j = \rho g \zeta_a H_j(K,\beta) \tag{23}$$

$$B_{ij} = \frac{\rho \omega K}{4\pi} \mathrm{Re} \int_0^{2\pi} H_i(K,\theta) H_j^*(K,\theta)\, d\theta \tag{24}$$

where $H_j(K,\theta)$ denotes the Kochin function in the radiation problem, expressed as

$$H_j(K,\theta) = \iint_{S_H} \left(\frac{\partial \phi_j}{\partial n} - \phi_j \frac{\partial}{\partial n} \right) e^{-Kz - iK(x\cos\theta + y\sin\theta)}\, dS \tag{25}$$

In terms of the Kochin function, the wave drift forces in the *x*- and *y*-axes proposed by Maruo [20] and the drift moment about the *z*-axis proposed by Newman [21] can be computed. The formulae for the first two components are written as

$$\left.\begin{aligned} \overline{F_x} &= \frac{\rho g \zeta_a^2}{8\pi} K \int_0^{2\pi} \left| H(K,\theta) \right|^2 \left(\cos\beta - \cos\theta \right) d\theta \\ \overline{F_y} &= \frac{\rho g \zeta_a^2}{8\pi} K \int_0^{2\pi} \left| H(K,\theta) \right|^2 \left(\sin\beta - \sin\theta \right) d\theta \end{aligned}\right\} \tag{26}$$

where

$$H(K,\theta) = H_7(K,\theta) - K \sum_{j=1}^{6} \frac{X_j}{\zeta_a} H_j(K,\theta) \tag{27}$$

$$H_7(K,\theta) = -\iint_{S_H} \phi_D \frac{\partial}{\partial n} e^{-Kz - iK(x\cos\theta + y\sin\theta)}\, dS \tag{28}$$

Wave elevations on free surface. The wave elevation on the free surface in the linear theory can be computed from

$$\frac{\zeta(x,y)}{\zeta_a} = \phi_0(x,y,0) + \phi_7(x,y,0) - K \sum_{j=1}^{6} \frac{X_j}{\zeta_a} \phi_j(x,y,0) \tag{29}$$

where the velocity potentials due to disturbance by a floating body can be computed from

$$\phi_7(P) = -\iint_{S_H} \phi_D(Q) \frac{\partial}{\partial n_Q} G(P;Q)\, dS(Q) \tag{30}$$

$$\phi_j(P) = \iint_{S_H} \left\{ n_j(Q) - \phi_j \frac{\partial}{\partial n_Q} \right\} G(P;Q)\, dS(Q) \tag{31}$$

where $P = (x,y,0)$ is a point on the free surface.
In the HOBEM, these velocity potentials can be computed by using the shape function and the solutions of the velocity potentials at nodal points. The integrals in Eqs. (30) and (31) can be evaluated by summation over all panels, on which element computations can be done using the same scheme for the coefficients shown in Eqs. (17) and (18), with P placed on the free surface.

The present study is concerned with the transmission and reflection waves by a floating breakwater. The transmission wave is defined by the wave in the lee side, propagating in the same direction as that of the incident wave. However, the reflection wave must be defined as the wave on the weather side, propagating to the opposite direction. Thus, the incident-wave term $\phi_0(x,y,0)$ in Eq. (29) is subtracted from Eq. (29) in numerical computations for the reflection wave.

3. Results and Discussion

Previous results. From a previous study [11], a 2D shape that has the optimal performance was obtained. The main criterion used for determining the performance of a model was the wave transmission amplitude. The smaller the wave transmission, the higher the performance was leveled.

The shape and dimensions of the 2D model in non-dimensional form. The performance of the model in terms of wave transmission compared to a simple rectangular box performance is shown again in Fig. 4 for reference.

In Fig. 4, a significant performance improvement can be seen in almost the entire frequency range except in the very long wavelength region. A larger body dimension is needed to improve this region. Please refer to Mahmuddin and Kashiwagi [11] for more discussion of this result.

Based on the 2D shape shown in Fig. 3, a 3D model shape is constructed by extruding it in the longitudinal direction (along *x*-axis) as shown in Fig. 5. The transverse section shape is the same as that in Fig. 3 and uniform in the longitudinal *x*-direction with its length denoted as *L*. Following the previous study, two body lengths will be analyzed: *L/B=2.0* and *20.0*, which represent shorter and longer bodies, respectively.

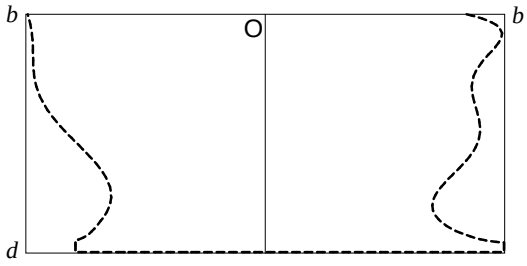

Figure 3. 2D Model Optimized Shape

Table 1. Dimensions of Optimized 2D Model

Notations	Unit
Maximum breadth ($B=2b$)	2.0
Draft (d)	1.0
Center of Gravity (OG)	0.82
Roll gyrational radius (KZZ)	0.614

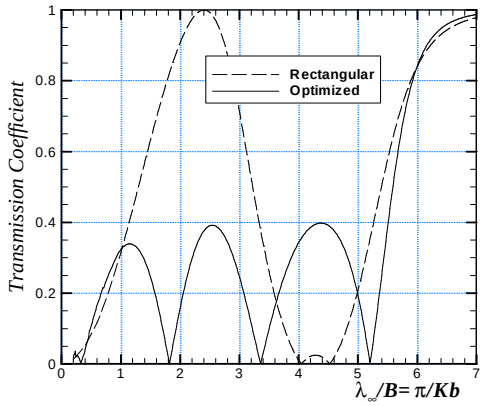

Figure 4. Transmission Coefficients of Optimized 2D and Rectangular Model

In the computations, following the 2D analysis carried out previously, half of the maximum breadth ($b = B/2$) is used for nondimensionalization. Moreover, in the previous studies [11,12], the incident angle β of a regular incoming wave is set equal to $\beta = -90$ degrees so that the situation corresponds to the 2D case and the results for the body motions and the reflection and transmission wave coefficients can be compared with 2D results.

Performance in oblique waves. In the present study, two incident wave angles are investigated, β_1=–112.5 and β_2=–157.5, as illustrated in Fig. 6. β_1 represents the case when the incident wave is the approaching beam wave, and β_2 represents the case when the incident wave is the approaching head wave.

For the sake of conciseness, only the computation results for the body motion amplitudes and the wave transmission coefficients for the free motions case are shown in the present study.

To evaluate the model's performance, six measurement positions are defined along the *y*-axis (the centerline of the body); those are three points in the lee side ($y/b = -4$, -10, and -18) and three points in the weather side ($y/b = 4$, 10, and 18) as shown in Fig. 7.

Based on the settings, computations are performed for a specific wavelength region. The computation results of the body motion amplitudes for β_1 case compared to the 2D case are shown in Figs. 8 and 9.

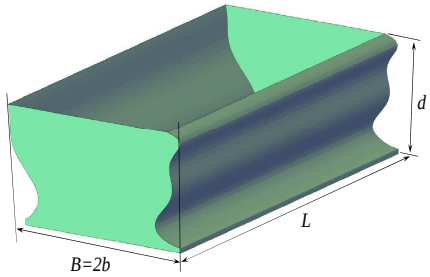

Figure 5. 3D Model Shape

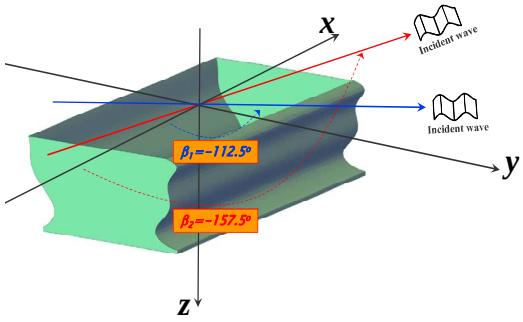

Figure 6. Incident Wave Angles Set

In Fig. 8, in the case of the incident wave as the approaching beam wave, the body motions' amplitude is similar in tendency and magnitude to those of the shorter body length, as shown in Fig. 8(a), but have a significantly smaller amplitude for the longer body compared to the 2D case, as shown in Fig. 8(b). The small body motion amplitudes is caused by a decrease in the wave-exciting forces especially for the sway, heave, and roll modes. These forces influence body motions more than the other modes because the body is elongated along the *x*-axis.

The body motion amplitudes for the second case are shown in Fig. 9. From Fig. 9, it can be seen that except for the heave motion, the magnitude and the tendency are different compared to the 2D case. In addition, in the β_2 case, the body motion amplitudes become smaller than the β_1 case for a longer body, as shown in Fig. 9(b). This is because the influential wave exciting forces (sway, heave, and roll) become smaller as in the previous case. They are even getting smaller as the incident wave the approaching head wave, which make the body motions even smaller as well.

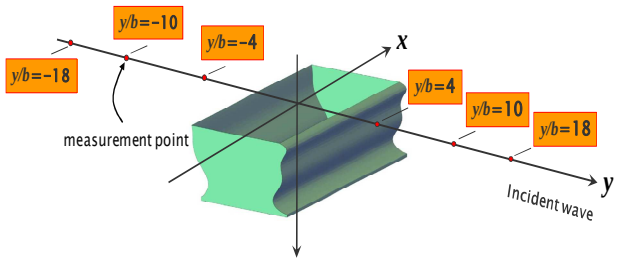

Figure 7. Measurement Positions of Wave Elevation

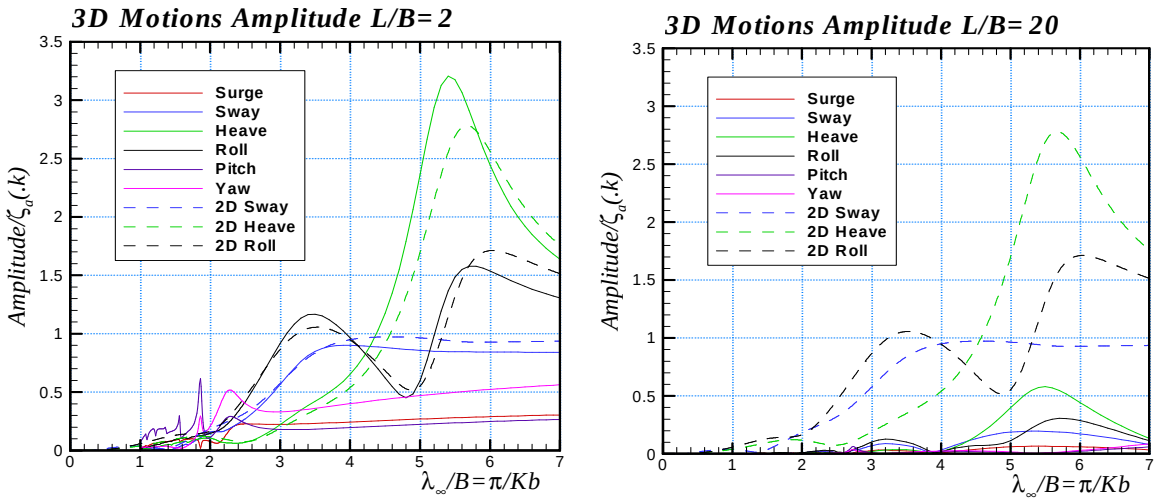

Figure 8. Body Motion Amplitudes for β_1 Case

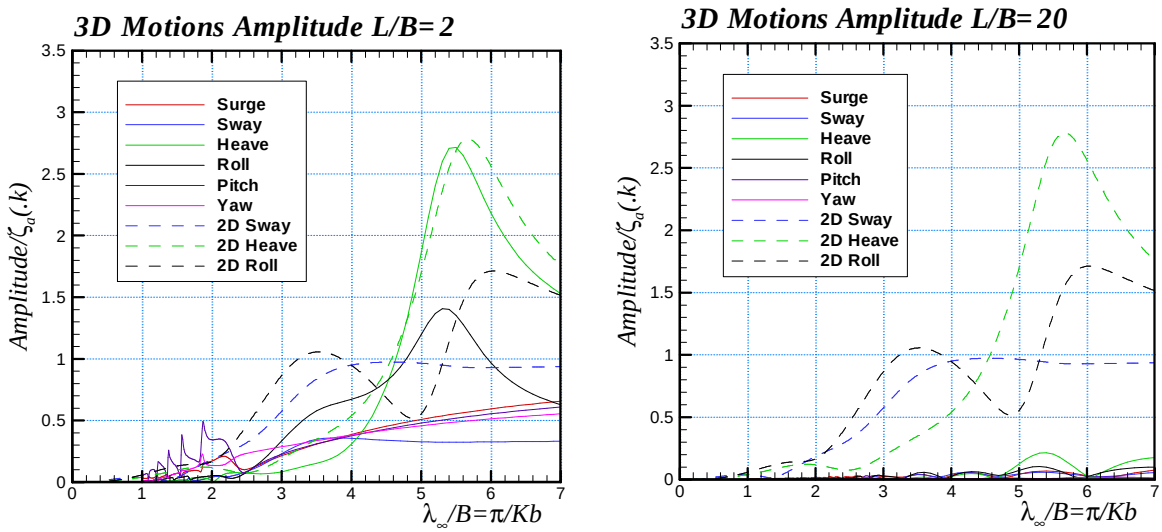

Figure 9. Body Motion Amplitudes for β_2

The performance in terms of the transmitted wave for the β_1 case can be plotted as follows. In Fig. 10, the transmitted wave fluctuates for a shorter body case especially in the short wavelength region as shown in Fig. 10(a). This happens because for a short body length, a significant amount of the incoming incident wave is transmitted to lee side. This is not true for the longer body dimension, as shown in Fig. 10(b).

In addition, regular variations are observed in the shorter wavelength region for both results. These variations are caused by irregular frequencies. A method for removing these irregular frequencies has been implemented by placing additional points on the free surface as explained in the previous section, but this remedy is insufficient. However, the irregular frequencies are not a fatal problem in discussing the results because the mean line of the regular variations is the expected result. The computation results for β_2 case are shown in Fig. 11.

From the results, it can observed that the transmission coefficients for the shorter body case are similar in magnitude and tendency except at *y/b=–10* as shown in Fig. 11(a). For a longer body, quite differently from the β_1 case, the tendency is similar, but the magnitude is larger compared to the β_1 case results. This is because

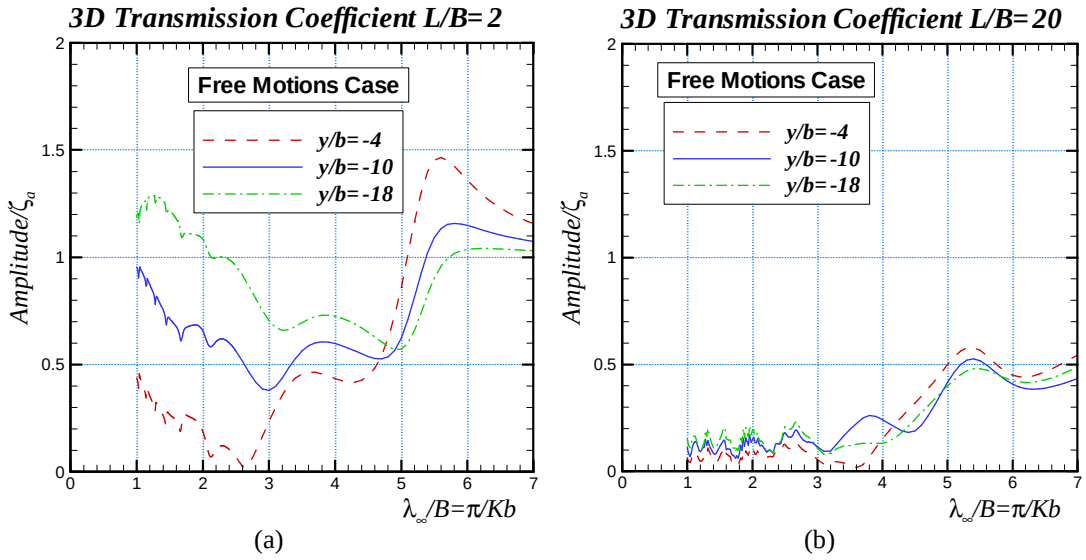

Figure 10. Transmitted Waves Amplitude for β_1

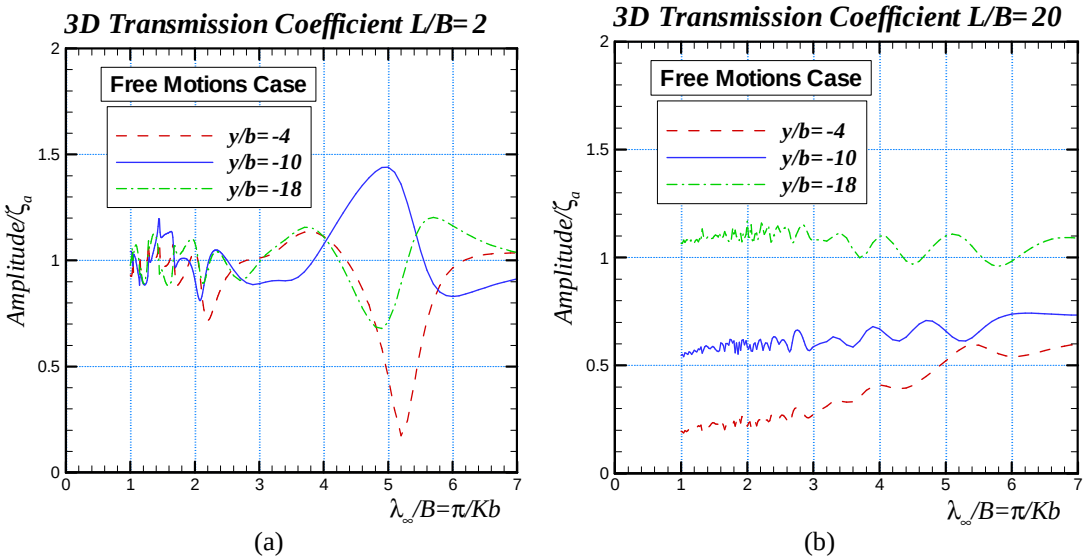

Figure 11. Transmitted Waves Amplitude for β_2

more waves are transmitted to the lee side compared to the β_1 case due to the incident wave angle value, which is an approaching head wave. From the computation results shown in Figs. 10 and 11, it can be concluded that in oblique waves, the transmission coefficient varies depending on the measurement position.

To observe more closely, the wave field around the floating breakwater is also computed. Because of limited space, only the results for a longer body (*L/B=20.0*) are shown and discussed. Two wavelengths are computed: λ/B=3.0 to represent a relatively shorter wavelength and λ/B=6.0 to represent a longer wavelength.

The computation result for the shorter wavelength λ/B=3.0 for β_1 is plotted and shown in Fig. 12. In Fig. 12, the lee side is much calmer even though the body moves freely to respond to the incident wave. The optimal performance obtained in 2D can also be obtained for the 3D case when the body length is long enough.

For the longer wavelength λ/B=6.0, the result is shown in Fig. 13. In Fig. 13, only a small calm area is observed in the lee side while other areas has a larger amplitude. This is because the wavelength is relatively longer. This result is reasonable by considering the result shown in Fig. 4 where the transmission wave amplitude is relatively larger around wavelength λ/B=6.0.

The computation results for β_2 case are shown in Fig. 14(a) and (b). In these figures, the calmer area is much smaller compared to the result shown in Figs. 12 and 13. This is because when the wave is the approaching head, more waves will be transmitted to the lee side of the body than in the previous case.

Moreover, the wave drift forces computed using Eq. (26) are shown in Fig. 15.

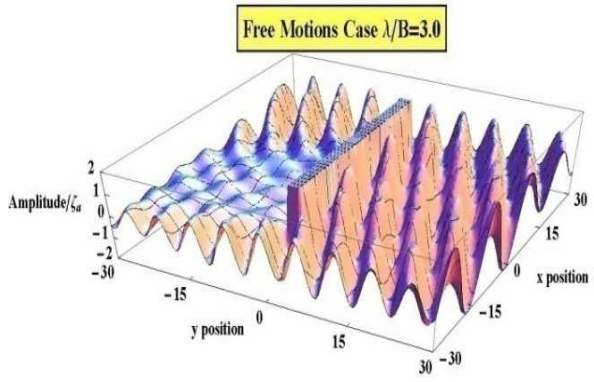

Figure 12. Wave Field for β_1, λ/B=3.0

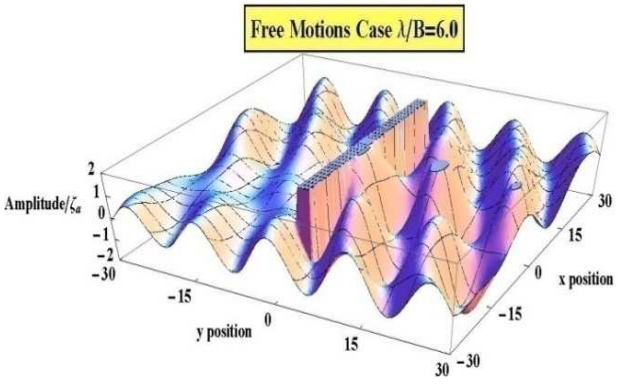

Figure 13. Wave field for β_2, λ/B=6.0

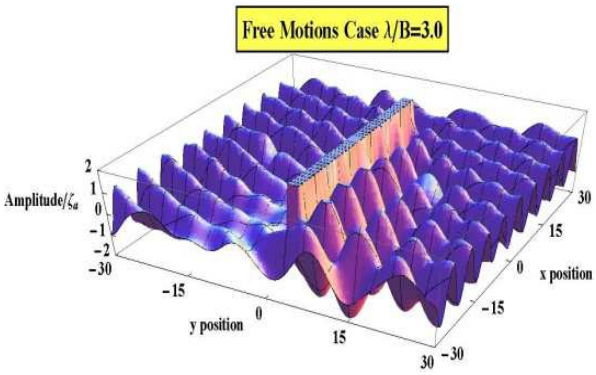

(a)

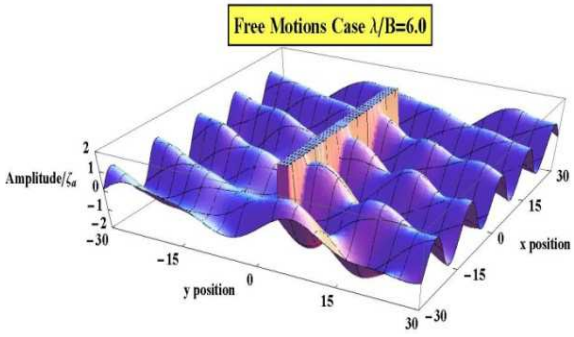

(b)

Figure 14. Wave field for β_2

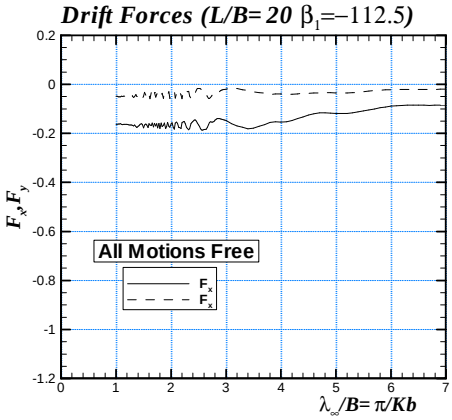

(a)

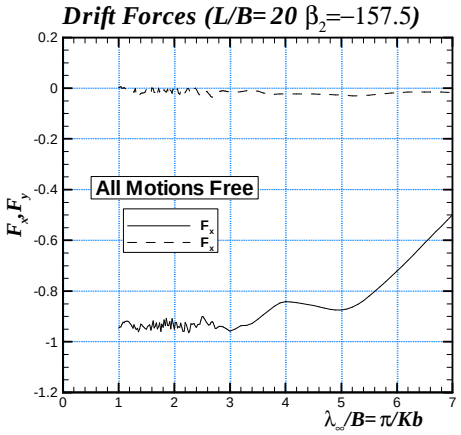

(b)

Figure 15. Drift Forces for *L/B=20.0*

The β_1 case computation result is shown in Fig. 15(a), and the β_2 case result is shown in Fig. 15(b). The computation result for the drift forces is useful information for mooring design.

4. Conclusions

From this study, several important points can be concluded. First, the 3D wave effects can be verified by comparing shorter and longer body computation results. In addition, the body motion amplitudes are smaller in oblique waves. Moreover, the performance of the model in oblique waves depends on the position of measurement, and the optimum performance in 2D case can also be realized in the 3D oblique wave case. In addition to those conclusions, drift forces was also computed and shown in the present study as information for mooring design.

References

[1] J.S. Mani, J. Waterway, Port, Coastal Ocean Eng. 117/2 (1991) 105.
[2] M.R. Gesraha, Appl. Ocean Res. 28/5 (2006) 327.
[3] H.Y. Wang, Z.C. Sun, Ocean Eng. 37/5 (2010) 520.
[4] S.A. Sannasiraj, V. Sundar, R. Sundaravadivelu. Ocean Eng. 25/1 (1998) 27.
[5] A.N. Williams, H.S. Lee, Z. Huang, Ocean Eng. 27/3 (2000) 221.
[6] K. Murali, K.S. Mani, J. Waterway, Port, Coastal Ocean Eng. 123/4 (1997) 172.
[7] M. Kashiwagi, H. Yamada, M. Yasunaga, T. Tsuji, Int. J. Offshore Polar Eng. 17/1 (2007) 39.
[8] M.A. Rahman, N. Mizutani, K. Kawasaki, Coastal Eng. 53/10 (2006) 799.
[9] S. Koshizuka, A. Nobe, Y. Oka, Int. J. Numerical Methods in Fluids. 26 (1998) 751.
[10] W. Koo, Ocean Eng. 36/9 (2009) 723.
[11] F. Mahmuddin, M. Kashiwagi, Proc. of 22nd Int. Society of Offshore and Polar Engineers, Rhodes Island, Greece, 2012, p.1263.
[12] M. Kashiwagi, F. Mahmuddin, Proc. of 22nd Int. Society of Offshore and Polar Engineers, Rhodes Island, Greece, 2012, p.1271.
[13] R.A. Dalrymple, M.A. Losada, P.A. Martin, J. Fluid Mech. 224 (1991) 625.
[14] I.H. Cho, S.T. Kee, M.H. Kim, Appl. Ocean Res. 19/3 (1997) 171.
[15] J. Wu, P.L.F. Liu, Appl. Ocean Res. 10/2 (1998) 66.
[16] Y.H. Zheng, Y.M. Shen, Y.G. You, B.J. Wu, D.S. Jie, Ocean Eng. 33/1 (2006) 59.
[17] M. Kashiwagi, Bulletin Research Institute for Applied Mechanics, Kyushu University Japan, 1995, p.83.
[18] M. Kashiwagi, 3D Boundary Element Method, Seizando Shoten, Co. Ltd., 2003.
[19] T. Haraguchi, S. Ohmatsu, Trans. West-Japan Soc. Naval Architect. 66 (1983) 9.
[20] H. Maruo, J. Ship Res. 4/3 (1960) 1.
[21] J. Newman, J. Ship Res. 1/1 (1967) 51.